

THE BLACK HOLE MASSES AND EDDINGTON RATIOS OF TYPE 2 QUASARS

M. Z. KONG¹ AND LUIS C. HO^{2,3}

¹*Department of Physics, Hebei Normal University, No.20 East of South 2nd Ring Road, Shijiazhuang 050024, China*

²*Kavli Institute for Astronomy and Astrophysics, Peking University, Beijing 100871, China*

³*Department of Astronomy, School of Physics, Peking University, Beijing 100871, China*

ABSTRACT

Type 2 quasars are an important constituent of active galaxies, possibly representing the evolutionary precursors of traditionally studied type 1 quasars. We characterize the black hole mass (M_{BH}) and Eddington ratio ($L_{\text{bol}}/L_{\text{Edd}}$) for 669 type 2 quasars selected from the Sloan Digital Sky Survey, using black hole masses estimated from the $M_{\text{BH}} - \sigma_*$ relation and bolometric corrections scaled from the extinction-corrected [O III] $\lambda 5007$ luminosity. When stellar velocity dispersions cannot be measured directly from the spectra, we estimate them from the core velocity dispersions of the narrow emission lines [O II] $\lambda\lambda 3726, 3729$, [S II] $\lambda\lambda 6716, 6731$, and [O III] $\lambda 5007$, which are shown to trace the gravitational potential of the stars. Energy input from the active nucleus still imparts significant perturbations to the gas kinematics, especially to high-velocity, blueshifted wings. Nonvirial motions in the gas become most noticeable in systems with high Eddington ratios. The black hole masses of our sample of type 2 quasars range from $M_{\text{BH}} \approx 10^{6.5}$ to $10^{10.4} M_{\odot}$ (median $10^{8.2} M_{\odot}$). Type 2 quasars have characteristically large Eddington ratios ($L_{\text{bol}}/L_{\text{Edd}} \approx 10^{-2.9} - 10^{1.8}$; median $10^{-0.7}$), slightly higher than in type 1 quasars of similar redshift; the luminosities of $\sim 20\%$ of the sample formally exceed the Eddington limit. The high Eddington ratios may be consistent with the notion that obscured quasars evolve into unobscured quasars.

Keywords: galaxies: active — galaxies: nuclei — galaxies: Seyfert — quasars: emission lines

arXiv:1804.09852v1 [astro-ph.GA] 26 Apr 2018

1. INTRODUCTION

The classical unified model of active galactic nuclei (AGNs) has served as a useful framework for synthesizing a wide range of observations (Antonucci 1993; Urry & Padovani 1995; Netzer 2015). In the simplest version of this model, the orientation of the central engine with respect to the viewer plays a major role in determining the observed characteristics, and hence classification, of AGNs. In particular, obscuration along the line-of-sight by a parsec-scale dusty torus dictates whether or not emission from the broad-line region is directly visible: unobscured type 1 sources exhibit broad permitted lines with velocity widths [full width at half maximum (FWHM)] $\gtrsim 1000 \text{ km s}^{-1}$, whereas obscured type 2 sources display only narrow emission lines. Within this framework, both types are intrinsically the same.

In recent years, however, it has become increasingly clear that the conventional, purely orientation-based unified model cannot account for the full diversity of the AGN population. Nor is it reasonable that it should. Accretion onto a central supermassive black hole (BH) powers AGNs. To the extent that the general galaxy population certainly evolves strongly with cosmic epoch, so, too, must the population of active galaxies, as BHs coevolve with their hosts (Kormendy & Ho 2013). The regime of low mass accretion rates (Ho 2008) offers the most dramatic examples of departures from the “standard” paradigm. At the lowest accretion rates, the obscuring torus—indeed, even the broad-line region itself—disappears (Elitzur & Ho 2009; Elitzur et al. 2014). Although less well-studied, “intrinsic” type 2 AGNs also emerge under conditions of higher accretion rates (e.g., Ho et al. 2012; Miniutti et al. 2013; Elitzur & Netzer 2016; Bianchi et al. 2017; Shu et al. 2017). Furthermore, in the merger-driven picture of quasar evolution (Sanders et al. 1988; Hopkins et al. 2006), dust-obscured (type 2) AGNs arise not simply from geometric viewing angle effects but instead as a direct consequence of a particular evolutionary phase, characterized by different, physically distinct conditions on both large and small scales. In other words, in the evolution-based model type 1 and type 2 AGNs are *not* intrinsically the same.

The evolutionary scenario linking type 1 and type 2 AGNs should manifest itself most readily in sources of high luminosity. During the past 15 years, increasing attention has been drawn to a population of type 2 quasars, especially the large samples uncovered systematically at optical wavelengths from the Sloan Digital Sky Survey (SDSS). Zakamska et al. (2003) identified 291 objects with redshifts $0.037 < z < 0.83$ based on standard optical diagnostic emission-line intensity ratios that place them in the category of AGNs. These objects have sufficiently narrow (FWHM $< 2000 \text{ km s}^{-1}$) permitted lines that make them likely candidates for type 2 sources, and, at the same time, about 50% of them have high enough [O III] $\lambda 5007$ luminosities ($> 3 \times 10^8 L_{\odot}$) that, when translated to equivalent *B*-band absolute magnitudes, qualify them as quasars by the historical criterion of $M_B < -23 \text{ mag}$ (Schmidt & Green 1983). Following a similar method, Reyes et al. (2008) expanded the SDSS sample to 887 candidates, the largest catalog to date of optically selected low-to-moderate redshift type 2 quasars¹. More recently, Alexandroff et al. (2013) further used SDSS to extend the selection of type 2 quasars to $2 < z < 4.3$.

What are the basic properties of type 2 quasars, and how do they compare with those of the more traditionally studied type 1 quasars? A number of studies suggest that the host galaxies of the two types of quasars indeed appear to differ. Relative to their type 1 counterparts, type 2 quasars seem to have elevated star formation rates (Kim et al. 2006; Zakamska et al. 2008, 2016), a higher incidence of tidal disturbances (Bessiere et al. 2012), and lower halo masses (Ballantyne 2016). Type 2 quasars also have a higher frequency of flat-spectrum radio cores (Lal & Ho 2010).

BH mass is one of the most fundamental physical parameters for AGNs. Also of interest for understanding the evolutionary state and the interconnections between different AGN populations is their Eddington ratio², which, too, relies on knowledge of the BH mass. Significant progress has been made in developing methods to derive BH masses for type 1 AGNs, through either reverberation mapping of broad emission lines (e.g., Kaspi et al. 2000) or empirically calibrated formalisms that use single-epoch spectra (e.g., Greene & Ho 2005b; Vestergaard & Peterson 2006; Ho & Kim 2015). These techniques, however, cannot be applied to narrow-line AGNs. Apart from a few rare instances in which BH masses in active galaxies can be measured directly through spatially resolved kinematics (see review in Kormendy & Ho 2013), in general we must resort to indirect methods to estimate BH masses for type 2 AGNs, principally through the well-known correlations between BH mass and host galaxy bulge stellar mass or velocity dispersion. These empirical relations, of course, were established originally for inactive galaxies at $z \approx 0$ (e.g., Tremaine et al. 2002; Häring & Rix 2004). When applying these relations to more active systems and especially at higher redshift, we implicitly assume

¹ Reyes et al. (2008) adopt a slightly modified luminosity criterion of $L_{[\text{O III}] \lambda 5007} > 2 \times 10^8 L_{\odot}$.

² The Eddington ratio is defined as $L_{\text{bol}}/L_{\text{Edd}}$, with L_{bol} the bolometric luminosity and $L_{\text{Edd}} = 1.26 \times 10^{38} (M_{\text{BH}}/M_{\odot}) \text{ erg s}^{-1}$, with M_{BH} the mass of the BH.

that (1) AGNs obey the same empirical scaling relations as local inactive galaxies, (2) these relations do not evolve with redshift, or (3) any potential redshift dependence can be corrected.

In this paper, we investigate the possibility of estimating BH masses for type 2 quasars using the $M_{\text{BH}} - \sigma_*$ relation (Ferrarese & Merritt 2000; Gebhardt et al. 2000). We proceed in two steps. Using the SDSS-selected sample of type 2 quasars from Reyes et al. (2008), we directly measure σ_* for a subset of sources having spectra of sufficiently high quality with detectable stellar features. For the majority of the sample for which these conditions could not be met, we estimate σ_* indirectly from the widths of their nebular emission lines. In AGNs of lower luminosity, it has been well-established that the kinematics of the ionized gas in the narrow-line region generally trace the virial motions of the stars of the host galaxy bulge (e.g., Whittle 1992; Nelson & Whittle 1996). In particular, in Seyfert galaxies the velocity width of [O III] $\lambda 5007$ traces σ_* , albeit with considerable scatter. Nelson (2000) found that σ_g , the velocity dispersion derived from ionized gas, can be used as a proxy to study the $M_{\text{BH}} - \sigma_*$ relation of AGNs. Greene & Ho (2005a) investigated the relation between gaseous and stellar kinematics for a large sample of SDSS-selected type 2 AGNs, showing that σ_g correlates best with σ_* when the gas velocities are derived from the core of the [O III] line, after removing its asymmetric wings. The $\sigma_g - \sigma_*$ relation also holds for the lower ionization lines [O II] $\lambda\lambda 3726, 3729$ and [S II] $\lambda\lambda 6716, 6731$. The analysis of Greene & Ho (2005a) focused on AGNs of relatively low luminosity, with $L_{[\text{O III}]} \lesssim 10^8 L_\odot$. Ho (2009) extended these results to sources of even lower luminosity, using [N II] $\lambda 6583$.

Is the $\sigma_g - \sigma_*$ relation applicable to the more powerful type 2 quasars? As the AGN luminosity increases, the narrow-line region gas may be increasingly susceptible to non-gravitational perturbations (e.g., radiation pressure), and it is unclear the extent to which the kinematics of the ionized gas still track the virial velocity of the underlying stellar gravitational potential. Greene et al. (2009) analyzed a sample of 111 type 2 quasars and found that the line widths of [O II] and [O III] exhibit no significant correlation with σ_* . This suggests that σ_g cannot be used to estimate BH mass for AGNs with luminosities in the range of quasars.

We investigate this problem with a new, independent analysis of the SDSS-selected sample of type 2 quasars of Reyes et al. (2008), taking special care to account for factors that may influence σ_g , such as asymmetries and other substructure in the line profile. Although the scatter is considerable, we find that, as in lower-luminosity AGNs, σ_g does still trace σ_* usefully in type 2 quasars. We use our newly derived $\sigma_g - \sigma_*$ relation, in combination with the latest $M_{\text{BH}} - \sigma_*$ relation, to estimate BH masses and Eddington ratios for the Reyes et al. (2008) sample of low-redshift type 2 quasars.

This paper is organized as follows. Section 2 discusses the sample selection. Section 3 presents measurements of σ_* and the analysis of the emission lines to derive σ_g . Section 4 compares σ_g and σ_* , discusses the prevalence of novirial motions in the narrow-line region, and applies the velocity dispersions to estimate BH masses and Eddington ratios. We summarize our main conclusions in Section 5. We adopt the following cosmological parameters: $\Omega_m = 0.3$, $\Omega_\Lambda = 0.7$, and $H_0 = 70 \text{ km s}^{-1} \text{ Mpc}^{-1}$.

2. SAMPLE

As one of the main purposes of our work is to measure stellar velocity dispersions and compare them with velocity dispersions derived from ionized gas, we need access to the rest-frame optical stellar continuum and a variety of well-measured strong emission lines. Thus, we focus on the sample of 887 type 2 quasars with redshifts $0.037 < z < 0.83$ from Reyes et al. (2008). The relatively low redshifts of the sample also help to minimize possible redshift evolution of the $M_{\text{BH}} - \sigma_*$ relation, an assumption critical to our application of the velocity dispersions to estimate BH masses for the sample.

We obtain the optical spectra of the sample from the seventh data release of SDSS (Abazajian et al. 2009). Some of the objects exhibit obvious double-peaked or otherwise conspicuous complex substructure in their emission-line core. The Reyes et al. sample contains a total of 126 sources with complex line substructure, among them 42 that have unambiguous double-peaked profiles. The line substructure is most evident in [O III], presumably because of its high signal-to-noise ratio (S/N), but in many cases it can also be seen in the weaker low-ionization lines. The objects with complex profile substructure span a similar range of [O III] luminosity and redshift as the parent sample (Figure 1). A variety of physical origins may give rise to kinematic complexity in the narrow-line gas. For instance, double-peaked profiles may be indicative of galaxy mergers, large-scale disk rotation, or outflows (e.g., Liu et al. 2010; Ge et al. 2012). The interaction of compact radio jets with the interstellar medium of the host galaxy can produce flat-topped cores and other profile substructure (e.g., Whittle et al. 1988; Gelderman & Whittle 1994). Whatever the case may be, these complexities will complicate the interpretation of the line widths and compromise our ability to use them to

trace virial velocities. We omit the 126 sources with complex profiles from our analysis of the emission-line widths, but we retain them for the purposes of measuring stellar velocity dispersions.

3. ANALYSIS

3.1. *Stellar Velocity Dispersions*

3.1.1. *Method*

The basic principle for measuring the line-of-sight stellar velocity dispersion of a galaxy through integrated spectroscopy is to estimate the degree to which the intrinsic stellar spectrum of the galaxy has been broadened by the internal motions (velocity dispersion) of its constituent stars. Traditional measurements are mostly based on Fourier or cross-correlation techniques (e.g., Sargent et al. 1977; Tonry & Davis 1979; Bender 1990), but more modern studies increasingly favor methods based on direct fitting of the spectra in pixel space (e.g., Kelson et al. 2000; Barth et al. 2002; Cappellari & Emsellem 2004; Greene & Ho 2006, hereafter GH06). One of the advantages of the latter method is that it is straightforward to exclude emission lines and other unwanted or bad pixels from the fit. The robustness of the fit can be evaluated readily from direct comparison of the broadened template spectrum with the galaxy spectrum.

We use the publicly available penalized pixel-fitting code `pPXF` of Cappellari & Emsellem (2004) to measure σ_* . Prior to analysis, we correct the SDSS spectra for foreground dust reddening, using the extinction values of Schlafly & Finkbeiner (2011) and the Galactic extinction curve of Cardelli et al. (1989). The spectra were then shifted to their rest frame, based on SDSS-derived redshifts. Our adopted values for the *V*-band Galactic extinction and redshift are listed in Table 1.

The `pPXF` program models the galaxy spectrum as

$$M_{\text{mod}}(x) = P(x) \left\{ \sum_{j=1}^N w_j [T_j(x) \otimes G(x)] \right\} + C(x), \quad (1)$$

where w_j is the fractional contribution of the j th stellar template $T_j(x)$ to the model flux, \otimes denotes convolution, $G(x)$ is a Gaussian broadening function with dispersion σ_m , and $P(x)$ is a Legendre polynomial that accounts for potential mismatches in shape between the galaxy and the templates, which might arise, for instance, from internal reddening, mismatches in stellar population, or residual calibration errors (e.g., GH06; Liu et al. 2009). The term $C(x)$ is a Legendre polynomial that represents any additional additive contribution, such as a power-law continuum from scattered light from the central AGN or a hot continuum from young O and B stars. The best-fit parameters are obtained by minimization of χ^2 using the nonlinear Levenberg-Marquardt algorithm implemented in the IDL package `mpfit`³ (Markwardt 2009).

The template $T(x)$ in principle should faithfully match the stellar population of the galaxy. However, in practice, it can be reasonably well represented by the spectrum of an optimally weighted linear combination of several stars or of even a well-chosen single star (e.g., Barth et al. 2002; GH06; Ho et al. 2009). There are many available libraries of stellar templates (e.g., Bruzual & Charlot 2003; Valdes et al. 2004; Sánchez-Blázquez et al. 2006), which have different wavelength coverage and spectra resolution. In light of the instrumental spectral resolution of SDSS (mean FWHM = 2.94 ± 0.31 Å over the region 4100–5400 Å used for our analysis of σ_* ; see below), the most suitable choice for our applications is the Indo-U.S. stellar spectral library (Valdes et al. 2004), which covers the wavelength range 3460–9464 Å at a spectral resolution of FWHM = 1.35 Å (Beifiori et al. 2011). Consistent with prior studies, a weighted linear combination of late-type (F, G, K, and M) red giant (luminosity class III) stars of near-solar metallicity provides a good match to the stellar continuum of the host galaxies. We also include an A-type dwarf (luminosity class V) star to account for those galaxies that have a substantial post-starburst stellar population.

As the template stars used in our fits were observed with a substantially higher spectral resolution than the SDSS science targets, the model velocity dispersion (σ_m) needs to be corrected to yield the intrinsic stellar velocity dispersion (σ_*) of the galaxy. We adopt $\sigma_*^2 = \sigma_m^2 + \sigma_{\text{inst},V}^2 - (\sigma_{\text{inst},S}/(1+z))^2$, where the instrumental resolution is $\sigma_{\text{inst},V} = 0.57$ Å for the Valdes et al. (2014) templates and $\sigma_{\text{inst},S} = 1.25$ Å for the SDSS spectra.

Careful consideration should be given to the choice of wavelength range over which to perform the fit, with the goal of avoiding regions contaminated by strong emission lines and other known sources of systematic bias. At optical

³ <http://purl.com/net/mpfit>

wavelengths, the Ca II $\lambda\lambda 8498, 8542, 8662$ infrared triplets are optimal for stellar dynamical work because of their relative insensitivity to stellar population (Dressler 1984) and AGN contamination (GH06), but they are shifted out of the SDSS bandpass and inaccessible to most of our sample. We do not consider Ca H+K $\lambda\lambda 3934, 3968$ because they are blended with [Ne III] $\lambda 3968$ and H ϵ $\lambda 3970$ (GH06), the latter being especially problematic when a strong A-star population is present. After much experimentation, we finally adopt 4100–5400 Å as the fitting region, but taking care to avoid strong emission lines (He II $\lambda 4686$, H β $\lambda 4861$, [O III] $\lambda\lambda 4959, 5007$). We exclude the Mg *Ib* $\lambda\lambda 5167, 5173, 5184$ triplets, which suffer from potential systematic effects due to [Mg/Fe] enhancement (Barth et al. 2002), but do include the G band at 4304 Å, after masking out H γ $\lambda 4340$ and [O III] $\lambda 4363$. Figure 2 shows a sample fit. Our chosen fitting regions are similar to those of Greene et al. (2009).

Kelson et al. (2000) found that σ_* is not very sensitive to $P(x)$ and $C(x)$, with differences of less than 1% in σ_* for Legendre polynomials of different orders. By contrast, similar tests by GH06 and Barth et al. (2002) indicate greater sensitivity of σ_* to the choice of polynomial order, particularly for fits performed over a relatively narrow wavelength range. Our own tests with the pPXF code confirm that the exact choice of polynomial order does not have a significant impact on σ_* (generally $\lesssim 2\%$ – 5%), so long as we avoid very low or high values. As a compromise, and for concreteness, we choose a third-order polynomial for $P(x)$ and $C(x)$.

To verify the robustness of our fitting method, we measured σ_* for the sample of 504 SDSS type 2 AGNs originally used by GH06 (their Figure 2) and performed a direct comparison between the two sets of measurements. The agreement is excellent (Figure 3). Defining the difference between the two sets of independent measurements by $\Delta\sigma_* \equiv \log \sigma_*(\text{ours}) - \log \sigma_*(\text{GH06})$, we find a mean value of $\langle \Delta\sigma_* \rangle = 0.002 \pm 0.05$, with little evidence for any systematic dependence on σ_* .

3.1.2. Error Estimates

The pPXF code returns formal (1σ) errors of $\sim 13\% \pm 6\%$ on σ_* for spectra with S/N greater than 15 (Cappellari & Emsellem 2004). However, in practice, errors on σ_* may be dominated by template mismatch or other sources of systematic uncertainties, especially for spectra of AGN host galaxies whose continuum may be contaminated by other sources of emission. The situation for type 2 AGNs is more favorable than that for type 1 AGNs (e.g., GH06), but even type 2 AGNs are not immune. For instance, the equivalent widths (EWs) of the stellar features may be diluted by a featureless continuum from scattered light from the nucleus (e.g., Liu et al. 2009; Alexandroff et al. 2013).

We perform a series of Monte Carlo simulations to evaluate the impact of template mismatch. We choose high-S/N (~ 90 per pixel near the G band) SDSS spectra of six inactive galaxies with $\sigma_* = 85, 114, 125, 178, 220, \text{ and } 360 \text{ km s}^{-1}$, roughly spanning the full range of σ_* encountered in our sample of type 2 quasars. In this study, we define the G band over 4285 – 4328 Å, with the continuum set to the midpoint of a power law connecting these two end points. The S/N is evaluated in the region 4400 – 4600 Å, which is relatively free from strong emission or absorption lines. We fit each spectrum 10^4 times, each trial randomly varying the set of five template stars (A-type dwarf plus a red giant of type F, G, K, and M) drawn from the Indo-U.S. stellar template library of Valdes et al. (2004). Figure 4 shows that the uncertainties on σ_* are always small, $\sim 4\% \pm 1\%$, with no systematic dependence on σ_* .

The S/N of the spectrum has a larger effect on σ_* measurements (Cappellari & Emsellem 2004). The strength (EW) of the stellar absorption lines will also matter. Furthermore, even for spectra of the same S/N and absorption-line EW, we anticipate that there may be systematic biases as a function of σ_* : for the same EW, a larger σ_* results in a broader, shallower spectral feature, which is more adversely affected by noise fluctuations and potential dilution by AGN continuum. We investigate these effects as follows. The above-described set of six high-S/N spectra of inactive galaxies have $\text{EW}(\text{G band}) \approx 10 \text{ \AA}$. We dilute the G band from the original strength of $\text{EW} \approx 10 \text{ \AA}$ to 1 \AA , in steps of 1 \AA , by artificially adding a constant continuum level to the spectrum. Poisson noise is introduced to produce a series of spectra with $\text{S/N} \approx 3 - 40$, in steps of 1 when $\text{S/N} < 10$, and in steps of 2 when $10 \leq \text{S/N} \leq 40$. In total, a grid of 230 pairs of EW and S/N was created for each of the six original input spectra, and for each pair we simulate 500 realizations.

Figure 5 summarizes the results of these simulations. As expected intuitively, the fractional error on σ_* , $\langle \delta\sigma_* \rangle \equiv \langle [\sigma_*(\text{input}) - \sigma_*(\text{output})] / \sigma_*(\text{input}) \rangle$, becomes enormous when both S/N and EW are low. On the other hand, $\langle \delta\sigma_* \rangle \lesssim 15\%$ – 20% when $\text{EW} \gtrsim 6 \text{ \AA}$ and $\text{S/N} \gtrsim 10$. The dependence on σ_* is weak, especially when $\sigma_* \gtrsim 200 \text{ km s}^{-1}$. We utilize the results of Figure 5 to empirically estimate the systematic uncertainty for our actual σ_* measurements. The final error budget for σ_* (Table 1) is the quadrature sum of three components: (1) the formal statistical uncertainty from

pPXF, (2) the systematic uncertainty due to potential template mismatch, which, based on the experiments described above, we assume to be 4%, and (3) the statistical uncertainty due to S/N and EW.

3.2. Gaseous Velocity Dispersions

A principal goal of this study is to evaluate whether and how well the velocity dispersion of the ionized gas in the narrow-line region of type 2 quasars traces the velocity dispersion of the stars in their host galaxies. Prior to measuring the emission lines, the stellar continuum should be properly modeled and subtracted, following essentially the same procedure described in Section 3 (see also Ho et al. 1997a). The main modification is that the wavelength range of the fit now extends from ~ 3700 to 7000 \AA in order to cover [O II] $\lambda\lambda 3726, 3729$, [O III] $\lambda\lambda 4959, 5007$, and [S II] $\lambda\lambda 6716, 6731$, the set of lines we use to measure the gaseous velocity dispersion (σ_g). This template fitting method provides a first-order estimate of the global continuum, but it is unlikely to achieve a high enough accuracy to yield a robust determination of the local continuum for all the emission lines of interest. We therefore sometimes need to apply a second-order correction to adjust the local continuum during the process of fitting the individual lines.

The narrow emission lines of AGNs generally have complex shapes that cannot be well described by a single Gaussian function. The profiles of most narrow lines, especially higher ionization lines such as [O III], often have an asymmetric blue, and at times red, wing (e.g., Whittle 1985; Veilleux 1991). Our sample of type 2 quasars exhibits similar trends. Although the profile asymmetry is most obvious for [O III] (most likely because of its high S/N), it is also frequently discernible for the lower ionization lines of [O II] and [S II] when the spectra have sufficiently high S/N. Following standard practice (e.g., Ho et al. 1997b; Greene & Ho 2005a), we fit⁴ each line with a single Gaussian component to represent the “core” (σ_g^c), and, if statistically warranted, we add another Gaussian component to reproduce the “wing” of the line. Some examples are shown in Figure 6. The wavelength separations of the three doublets are fixed to their laboratory values. We force the components of each doublet to have the same velocity profile, even though in actuality each of the two transitions of the [O II] and [S II] doublets has slightly different critical densities and hence can have mildly different velocity widths (Filippenko & Halpern 1984; Ho et al. 1996). We fix the flux ratio of [O III] $\lambda 5007$ /[O III] $\lambda 4959$ to the theoretical value of 3, but for the two densitometers, [O II] $\lambda 3729$ /[O II] $\lambda 3726$ is allowed to vary from 0.3 to 1.5, and [S II] $\lambda 6716$ /[S II] $\lambda 6731$ can range between 0.45 and 1.5 (Osterbrock 1989).

Apart from the emission-line widths derived from the above-described parametric fits, we also provide a simpler estimate of line width from a direct, non-parametric measurement of the intrinsic FWHM (i.e. after correction for instrumental resolution) of the line profile itself. Then, the Gaussian-equivalent velocity dispersion is $\sigma_m \equiv \text{FWHM}/2.35$. Instead of measuring FWHM directly from the data, which is affected by noise, it is more effective to calculate it from a model (noise-free) representation of the line profile. We construct the model by decomposing the original profile using a series of Gaussians, and then summing up the individual components. We use as many Gaussians as statistically necessary to fit the profile. In general two Gaussians are sufficient for each of the doublet lines of [O II] and [S II], but [O III] may occasionally require up to four to properly account for more extended wings. There is no physical meaning attached to any of the Gaussian components; they just serve as a convenient representation of the data. Lastly, as in Greene & Ho (2005a), we compute the second moment (σ_g^s) of the best-fit model to describe the width of the overall global line profile.

The core velocity dispersions and second moments for [O II], [S II], and [O III], corrected for the instrumental resolution of SDSS⁵, are listed in Table 1. The error budget for σ_g^c consists of three terms combined in quadrature: (1) a formal, statistical uncertainty (generally $\lesssim 5\%$) from `mpfit`; (2) a systematic uncertainty due to errors in the placement of the local continuum, and (3) a systematic uncertainty due to the choice of initial parameters for the multi-component fit. We estimate terms (2) and (3) through a series of Monte Carlo simulations by changing the initial fitting parameters. The error budget for σ_g^s includes only terms (2) and (3).

3.3. External Comparison

Greene et al. (2009) performed an independent analysis of the Reyes et al. (2008) sample, using a methodology very similar that employed in this work. They provide σ_* measurements for 111 objects, as well as FWHM values for [O II] and [O III]. Figure 7 directly compares our measurements with those of Greene et al. (2009). The agreement is reasonably good in the mean, although the scatter is relatively large for σ_* . The mean difference between the two sets

⁴ The fits are performed using the IDL code `mpfit`.

⁵ The average instrumental spectral resolution of SDSS for our sample is $\text{FWHM} = 2.54 \pm 0.30 \text{ \AA}$ for [O II], $3.03 \pm 0.35 \text{ \AA}$ for [O III], and $3.24 \pm 0.39 \text{ \AA}$ for [S II].

of measurements $\langle \Delta\sigma_* \rangle = -0.072 \pm 0.24$, where $\Delta\sigma_* \equiv \log \sigma_*(\text{ours}) - \log \sigma_*(\text{Greene} + 09)$. As for the emission-line widths, $\langle \Delta\text{FWHM} \rangle = 0.012 \pm 0.04$ for [O II] and -0.002 ± 0.03 for [O III].

3.4. Final Set of Measurements

Out of the original sample of 887 sources, 449 (51%) have spectra with S/N > 3 per pixel and detectable G band with EW larger than 3 Å. While we succeeded to measure σ_* for most of these, many of the uncertainties are rather large. For our subsequent analysis, we only make use of the subset of objects with σ_* measurements that are clearly in excess of the SDSS spectral resolution ($\sim 70 \text{ km s}^{-1}$) and that have fractional uncertainties $\leq 20\%$. Only 219 objects (25% of the original sample) satisfy these criteria. The number of σ_* measurements increases to 281 if we relax the fractional uncertainty to 30%. As for the gaseous line widths, after excluding the 126 objects with kinematically complex core structure, 594 of the remaining 761 objects have a σ_g^c measurement with an intrinsic value larger than 70 km s^{-1} and a fractional uncertainty $\leq 20\%$ for at least one of the three principal emission lines ([O II], [O III], and [S II]). The number of σ_g^c measurements increases to 697 if the fractional uncertainty is relaxed to 30%. The majority of the sample has useful measurements of σ_g^s , at least for [O III], the strongest line, but often also for [O II] and [S II]. The final set of velocity measurements is given in Table 1. We only list measurements with fractional uncertainties less than 30%.

In total, 142 objects have measurements with fractional uncertainties $\leq 20\%$ for both σ_* and σ_g^c for at least one emission line. Not surprisingly, they are drawn predominantly from the portion of the parent sample with the lowest luminosities (median $L_{[\text{O III}]}$ $\approx 10^{42.5} \text{ erg s}^{-1}$) and redshifts (median $z \approx 0.2$), although on average they are still more distant and much more luminous than the sample of type 2 AGNs of Greene & Ho (2005a; Figure 1).

4. RESULTS

4.1. Comparison Between Velocity Dispersions of Stars and Ionized Gas

Figure 8 begins with a comparison between σ_* and σ_g , defined simply as FWHM/2.35 (appropriate for a Gaussian function), where FWHM is measured from the total line profile of [O II] (166 objects), [S II] (154 objects), and [O III] (169 objects). It is clear that most of the gas velocities are significantly larger than the stellar velocities, and there is little correlation between the two quantities. The average value and standard deviation of $\langle (\text{FWHM}/2.35)/\sigma_* \rangle$ is 1.17 ± 0.38 , 1.15 ± 0.35 , and 1.11 ± 0.40 for [O II], [S II], and [O III]. This is consistent with the conclusion of Greene et al. (2009) and Liu et al. (2009), who parameterized the gas velocity dispersion in the same way. The situation is even more extreme for σ_g^s , the second moment of the line, which is maximally sensitive to the wings of the profile. Figure 9a shows that $\sigma_g^s \gtrsim \sigma_*$ for nearly all the type 2 quasars, some by very significant amounts. The range of σ_g^s/σ_* spans 0.65 to 6.01, with $\langle \sigma_g^s/\sigma_* \rangle = 1.73 \pm 0.75$, 1.66 ± 0.80 , and 1.85 ± 0.88 for [O II], [S II], and [O III], respectively. In other words, the narrow lines of type 2 quasars invariably have highly non-Gaussian, extended, usually blue asymmetric wings. Note that for lower-luminosity AGNs, only the high-ionization line [O III] shows blue asymmetry (Greene & Ho 2005a; Ho 2009; Figure 9a).

By contrast, once we remove the line wings and focus only on the core of the emission-line profile (σ_g^c), the situation improves dramatically (Figure 9b). The gas velocities become comparable to the stellar velocities, and the scatter decreases. We find $\langle \sigma_g^c/\sigma_* \rangle = 1.06 \pm 0.32$, 0.99 ± 0.32 , and 1.00 ± 0.36 for [O II], [S II], and [O III]. Because of the small sample size, limited dynamic range, and large measurement uncertainties, the correlation between σ_* and σ_g^c is not statistically strong for the type 2 quasars alone. The Spearman's rank correlation coefficients are $\rho = 0.32$ and 0.34 for [O II] and [S II], respectively, with a probability for the null hypothesis of no correlation of $P_{\text{null}} \approx 0.02$; for [O III], $\rho = 0.17$ and $P_{\text{null}} = 0.1$. The lower luminosity sources of Greene & Ho (2005a)⁶ behave very similarly: $\langle \sigma_g^c/\sigma_* \rangle = 1.13 \pm 0.38$, 1.11 ± 0.35 , and 1.01 ± 0.35 . For both samples combined, we obtain $\langle \sigma_g^c/\sigma_* \rangle = 1.13 \pm 0.38$, 1.11 ± 0.35 , and 1.00 ± 0.35 . Now the $\sigma_* - \sigma_g^c$ relation is highly statistically significant, with $\rho = 0.43$, 0.46 , and 0.42 and $P_{\text{null}} < 10^{-6}$ for [O II], [S II], and [O III]. Among the three emission lines considered, σ_g^c for [S II] formally correlates strongest with σ_* , and the ratio of the two has a somewhat smaller scatter. By comparison, [O III] exhibits the poorest performance. As Greene & Ho (2005a) remarked, a possible explanation is that [O III], which has a significantly higher critical density than [O II] and [S II], originates from closer to the nucleus if the narrow-line region is density-stratified and hence has profile wings of higher velocity.

⁶ As in our analysis, Greene & Ho (2005a) decomposed [O III] using two Gaussians, one for the core and another for the wing; here we use their core component of [O III]. They only fit a single Gaussian for each of the doublet components of [O II] and [S II], but in view of the relative weakness of the wing component for the low-ionization lines in low-luminosity sources (see, e.g., Figure 9a), their single component is analogous to the core component of type 2 quasars.

We verified that the above results are quite stable with respect to our particular choice of cut on data quality. Restricting the velocity dispersions to those with fractional errors $\leq 10\%$ reduces the scatter of $\langle \sigma_g^c / \sigma_* \rangle$ from ~ 0.35 to ~ 0.25 for the type 2 quasar, at the expense of shrinking the sample, whereas relaxing the fractional errors to 30% results in a moderate increase of scatter on $\langle \sigma_g^c / \sigma_* \rangle$ but there is little effect on the significance of their statistical correlation. Our analysis shows that, as in lower-luminosity AGNs (e.g., Nelson & Whittle 1996; Greene & Ho 2005a; Ho 2009), the kinematics of the narrow-line region gas in type 2 quasars also approximately traces the virial motions of the stars in the central regions of their host galaxies. As such, the line widths of the narrow emission lines serve as an effective, economical substitute for the bulge stellar velocity dispersion, which is difficult, and at times impossible, to measure. Consistent with Greene & Ho (2005a), we find that σ_g only tracks σ_* well when care is taken to remove the wings of the emission lines. Bian et al. (2006) reached a similar conclusion for a more limited number of type 2 quasars selected from the initial SDSS sample of Zakamska et al. (2003). For the three emission lines investigated here, the low-ionization line [S II] appears most promising. Its core velocity dispersion is, on average, essentially identical to σ_* , with a standard deviation of 32%. The next best candidate is [O II], followed by [O III], as a last resort. Although the [O II] doublet is only marginally resolved by SDSS, and its σ_g^c exhibits the largest deviation from σ_* , the deviation (6%) is systematic and therefore correctable, and its scatter (32%) is formally identical to that of [S II] (32%). Still, priority should be given to [S II] whenever possible, as [O II] emanates not only from the narrow-line region but also from extra-nuclear emission-line regions. [O II] is prominent in H II regions (e.g., Gallagher et al. 1989) and traces galaxy-wide star formation, even in AGN hosts (Ho 2005).

4.2. Nonvirial Motions: Dependence on AGN Properties

The vast majority of type 2 quasars emit narrow-line gas with large, blueshifted velocities, not only in the high-ionization tracer [O III], but also in the low-ionization species [O II] and [S II]. This is most clearly seen in the large, systematic, positive offsets between σ_g^s and σ_* (Figure 9a). While the core component of the emission lines much better traces the gravitational potential of the stars (Figure 9b), a small fraction of our sample ($\sim 4\%$) still exhibits [O III] core velocity dispersions in excess of 400 km s^{-1} , a couple as high as $\sim 1000 \text{ km s}^{-1}$. Such velocities certainly do not reflect the virial motions of any realistic host galaxy. The central stellar velocity dispersions of nearby galaxies rarely exceed 350 km s^{-1} (Sheth et al. 2003). Instead, these large, super-virial velocities most likely arise from substantial energy injection into the narrow-line region, presumably from the AGN, which affect even the core velocities of the narrow emission lines. Moreover, while the core gas velocities are close, they are not exactly identical, to the stellar velocities. Do the residuals of the $\sigma_g - \sigma_*$ relation depend on AGN properties? Greene & Ho (2005a; see also Bian et al. 2006) find that for [O III] the degree of offset between σ_* and σ_g^s , which is sensitive to the wing component of the line, statistically scales with the Eddington ratio. The wing component is more blueshifted with increasing Eddington ratio. However, even the core of the line profile can be affected. Ho (2009) finds that while gravity is the primary agent responsible for the velocity broadening of the core of the [N II] line, the Eddington ratio acts as a secondary driver of the $\sigma_g^c - \sigma_*$ relation: sources with higher Eddington ratios have systematically larger core line widths relative to σ_* . Optical AGN luminosity and radio power also correlate with excess gaseous velocities, although Eddington ratio appears to be the more dominant factor (Ho 2009).

To evaluate whether these effects also apply to type 2 quasars, we need to quantify the BH mass and bolometric luminosity. In the absence of broad emission lines, the only viable method to estimate BH masses for type 2 sources is to make use of empirical scaling relations between BH masses and the properties of their host galaxies established for local samples of inactive galaxies (Kormendy & Ho 2013). The most widely discussed correlations are those between BH mass and bulge stellar mass and stellar velocity dispersion. But challenges arise in connection with our intended current application to the SDSS-selected sample of type 2 quasars. First, the BH-bulge scaling relations (e.g., the $M_{\text{BH}} - \sigma_*$ relation) has been shown to hold—with reasonable choices for the virial factor f —mainly for nearby ($z \approx 0$) type 1 (broad-line) AGNs (e.g., Onken et al. 2004; Ho & Kim 2014). Our sample, by contrast, consists of type 2 AGNs at moderate redshift. In order to utilize the $M_{\text{BH}} - \sigma_*$ relation to estimate their BH masses, we must assume (1) that the $M_{\text{BH}} - \sigma_*$ relation applies to type 2 AGNs and (2) that we can neglect (or account for) its possible evolution with redshift, at least for the redshift range of our sample ($z \lesssim 0.8$). Du et al. (2017) investigated the virial factors for a handful of Seyfert 2 galaxies with hidden broad-line regions and concluded that they are statistically consistent with the average virial factors of type 1 AGNs. This implies that both type 1 and type 2 AGNs have broad-line regions of similar structure and kinematics. In the present context, it suggests—at least tentatively—that the $M_{\text{BH}} - \sigma_*$ relation can be applied to type 2 AGNs. The situation regarding the possible evolution of the $M_{\text{BH}} - \sigma_*$ relation

with redshift is unclear. On the one hand, a number of studies suggest that the zero point for the $M_{\text{BH}} - \sigma_*$ relation increases toward higher redshifts, typically by $\sim 0.3 - 0.5$ dex when $z \approx 0.4 - 0.6$ (Woo et al. 2006, 2008; Treu et al. 2007). On the other hand, Shen et al. (2015) argue that this apparent evolution largely reflects selection effects, while Kormendy & Ho (2013) show that the latest calibration of the local $M_{\text{BH}} - \sigma_*$ relation essentially offsets the previously reported evolution of zero point at moderate redshifts. Thus, in the following analysis, we assume that our sample of low-redshift type 2 quasars obeys the local $M_{\text{BH}} - \sigma_*$ relation. From Equation 5 of Kormendy & Ho (2013),

$$\log\left(\frac{M_{\text{BH}}}{10^9 M_{\odot}}\right) = -(0.500 \pm 0.049) + (4.429 \pm 0.295) \log\left(\frac{\sigma_*}{200 \text{ km s}^{-1}}\right). \quad (2)$$

This relation has an intrinsic scatter of 0.28 dex. Note that the above relation applies only to classical bulges and elliptical galaxies, not to pseudobulges or to galaxy samples that contain a mixture of bulge types⁷. Apart from a minority of the objects (Zhao et al. 2018), we do not have reliable bulge classifications for most of our sample. In the subsequent analysis, we adopt Equation (2) to derive BH masses, but in Section 4.3 we will examine the consequences of relaxing this assumption.

The [O III] $\lambda 5007$ line offers the most practical means of tracing the level of AGN activity for the current sample of optically selected type 2 quasars. It is common practice to use the [O III] luminosity to estimate the AGN bolometric luminosity, but considerable debate surrounds the proper bolometric correction, the role of extinction correction, and whether or not the bolometric correction is luminosity-dependent (e.g., Heckman et al. 2004; Netzer et al. 2006; Kauffmann & Heckman 2009; Lamastra et al. 2009; Stern & Laor 2012; Pennell et al. 2017; see discussion in Heckman & Best 2014). For concreteness, we adopt a constant bolometric correction of 600 (i.e., $L_{\text{bol}} = 600 L_{[\text{O III}]}$) to the extinction-corrected [O III] luminosity, following the recommendation of Kauffmann & Heckman (2009), with an uncertainty of ± 150 . For comparison, we will also consider the constant bolometric correction of 3500 for extinction-uncorrected [O III] luminosity originally advocated by Heckman et al. (2004), as well as the luminosity-dependent, extinction-corrected bolometric corrections of Lamastra et al. (2009), as parameterized by Trump et al. (2015). We estimate the internal extinction from the observed Balmer decrement, assuming an intrinsic value of $H\alpha/H\beta = 3.1$ appropriate for AGNs (Halpern & Steiner 1983) and the extinction curve of Cardelli et al. (1989). For objects for which the Balmer decrement could not be measured, we adopt the median value of $H\alpha/H\beta = 4.04$ obtained from the objects for which this quantity was measured.

Figure 10a shows the relation between $\Delta\sigma^s \equiv \log\sigma_g^s - \log\sigma_*$ and $L_{\text{bol}}/L_{\text{Edd}}$, both for our sample of type 2 quasars (red points) and for lower luminosity sample of Seyferts from Greene & Ho (2005a; small grey points). We consistently recalculate the black hole masses and bolometric luminosities of the Greene & Ho objects using the $M_{\text{BH}} - \sigma_*$ relation adopted in this work (Equation 2) and the bolometric correction of 600 for extinction-corrected [O III] luminosity⁸. The velocity residuals of all three transitions correlate positively and strongly with the Eddington ratio, both for the high-luminosity and low-luminosity samples. The combination of the lower luminosity Greene & Ho sources and our high-luminosity quasars provides the largest dynamic range in Eddington ratio, yielding the following functional dependence between $\Delta\sigma^s$ and $L_{\text{bol}}/L_{\text{Edd}}$ (black solid line in Figure 10a):

$$\Delta\sigma^s = \begin{cases} (0.106 \pm 0.004) \log(L_{\text{bol}}/L_{\text{Edd}}) + (0.255 \pm 0.009) & \text{for [O II]} \\ (0.093 \pm 0.004) \log(L_{\text{bol}}/L_{\text{Edd}}) + (0.222 \pm 0.009) & \text{for [S II]} \\ (0.149 \pm 0.005) \log(L_{\text{bol}}/L_{\text{Edd}}) + (0.392 \pm 0.010) & \text{for [O III]}, \end{cases} \quad (3)$$

with Spearman's rank correlation coefficients of $\rho = 0.43, 0.38,$ and 0.56 , respectively, and $P_{\text{null}} < 10^{-6}$. Greene & Ho (2005a) already presented the results for [O III] for type 2 Seyferts. Here we confirm that it extends to sources of even higher luminosity and Eddington ratio, and, moreover, that it also applies to the low-ionization lines [O II] and [S II].

More surprisingly, we find that even the *core* component of the lines are affected systematically by Eddington ratio (Figure 10b). The type 2 quasars exhibit the strongest correlation between $\Delta\sigma^c$ and $L_{\text{bol}}/L_{\text{Edd}}$ ($\rho = 0.66, 0.49,$ and 0.61 for [O II], [S II], and [O III]; $P_{\text{null}} < 10^{-6}$), but statistically significant correlations also exist for the lower-luminosity objects of Greene & Ho (2005a) alone ($\rho = 0.36, 0.32,$ and 0.14 for [O II], [S II], and [O III]; $P_{\text{null}} < 10^{-6}$), and for

⁷ She et al. (2017) provide a fit for the $M_{\text{BH}} - \sigma_*$ relation of all galaxies with reliable BH masses from Kormendy & Ho (2013), regardless of bulge type: $\log(M_{\text{BH}}/10^9 M_{\odot}) = (-0.68 \pm 0.05) + (5.20 \pm 0.37) \log(\sigma/200 \text{ km s}^{-1})$, with an intrinsic scatter of 0.44 dex.

⁸ The [O III] luminosities of Greene & Ho (2005a) were not corrected for internal extinction. For consistency with the conventions of our study, we applied an internal extinction correction to the luminosities of Greene & Ho (2005a) using Balmer decrements for their objects obtained from the JHU/MPA database (<https://wwwmpa.mpa-garching.mpg.de/SDSS>)

both samples combined ($\rho = 0.33, 0.26, \text{ and } 0.13$ for [O II], [S II], and [O III]; $P_{\text{null}} < 10^{-6}$). The sensitivity of σ_g^c to $L_{\text{bol}}/L_{\text{Edd}}$ echoes the findings of Ho (2009; overplotted as dotted line in the [O II] and [S II] panels of Figure 10b) based on the low-ionization line [N II] $\lambda 6583$, which extend the Eddington ratios down by ~ 2 orders of magnitude, to $L_{\text{bol}}/L_{\text{Edd}} \approx 10^{-5.5}$.

We looked for, but failed to find, any dependence between velocity excess (either $\Delta\sigma^s$ or $\Delta\sigma^c$) and [O III] luminosity or 20 cm radio power (available from the FIRST database; Becker et al. 1995). Greene & Ho (2005a) arrived at a similar conclusion for $\Delta\sigma^s$. The mildly significant correlation between $\Delta\sigma^c$ ([N II]) and H α luminosity and radio power seen by Ho (2009), which he considers to be secondary to the influence of Eddington ratio, may be masked by the larger measurement uncertainties of the present data.

4.3. Black Hole Masses and Eddington Ratios

One of the main objectives of this study is to evaluate the BH masses and Eddington ratios of type 2 quasars. We estimate BH masses using the $M_{\text{BH}} - \sigma_*$ relation (Equation 2). Having established that the kinematics of the narrow-line region in type 2 quasars largely tracks the virial velocities of the bulge, we use the velocity dispersion of the core component (σ_g^c) of the narrow lines to estimate σ_* whenever the latter is unavailable. We give preference to σ_g^c from [S II], followed by [O II], and then [O III]. We adjust the gas velocity dispersions by applying a small statistical zeropoint scaling correction: $\langle \sigma_g^c / \sigma_* \rangle = 0.99, 1.06, \text{ and } 1.00$ for [S II], [O II], and [O III]. As mentioned in Section 4.2, a small fraction of the objects have exceptionally large [O III] line widths of clearly non-gravitational origin. We omit these from the following analysis.

The BH masses of type 2 quasars range from $M_{\text{BH}} \approx 10^{6.5}$ to $10^{10.4} M_{\odot}$, with a median value of $10^{8.2} M_{\odot}$ (Figure 11a). Had we adopted the $M_{\text{BH}} - \sigma_*$ relation of She et al. (2017; see footnote 7), which does not distinguish between classical and pseudo bulges, the median BH mass would decrease by ~ 0.25 dex. The Eddington ratios span $L_{\text{bol}}/L_{\text{Edd}} \approx 10^{-2.9}$ to $10^{1.8}$, with a median value of $10^{-0.7}$ (Figure 11b). These BH masses and Eddington ratios are very similar to the results of Greene et al. (2009). The alternative [O III] bolometric corrections of Trump et al. (2015) yield a lower median $L_{\text{bol}}/L_{\text{Edd}}$ lower by ~ 0.2 dex, while Heckman et al.'s (2004) bolometric correction would lead to an increase of ~ 0.4 dex in the median $L_{\text{bol}}/L_{\text{Edd}}$. Figure 12 compares type 2 quasars with optically selected type 1 AGNs over the same redshift range ($z < 0.83$) studied by Shen et al. (2011). Roughly half of the type 1 sources have $L_{[\text{O III}]}$ $\gtrsim 2 \times 10^{42}$ erg s $^{-1}$, the lower limit threshold adopted for type 2 quasars (Reyes et al. 2008). The BH masses for the type 1 sources, taken directly from Shen et al. (2011), are based on single-epoch virial mass estimators using the broad H β or Mg II emission lines. For consistency with the type 2 sources, we also compute the bolometric luminosities of the type 1 sample using $L_{[\text{O III}]}$ from Shen et al., but in this instance we need to use the [O III] bolometric correction of Heckman et al. (2004) because extinction corrections are not available. Taken at face value, type 2 quasars cover a similar range of BH masses and Eddington ratios as type 1 quasars, with type 1 systems tending toward somewhat higher M_{BH} (median $10^{8.5} M_{\odot}$) and lower $L_{\text{bol}}/L_{\text{Edd}}$ (median $10^{-0.9}$). The lower-luminosity type 2 Seyferts of Greene & Ho (2005a) differ more dramatically from type 2 quasars (median $M_{\text{BH}} = 10^{7.9} M_{\odot}$; median $L_{\text{bol}}/L_{\text{Edd}} = 10^{-2.1}$), but this is a trivial consequence of sample selection (the optically selected type 2 quasars are required to meet the luminosity threshold of quasars).

Significant uncertainties and selection effects complicate the comparison between type 1 and type 2 quasars (e.g., BH mass estimation, bolometric corrections, dust extinction, etc), and we do not recommend taking too literally the numerical values for any individual object or of the apparent minor differences between the two quasar populations. Nevertheless, it is worth remarking that the bolometric luminosities for $\sim 20\%$ of the type 2 quasars formally exceed the Eddington limit, some by a significant margin; 11 objects (1.6%) have $L_{\text{bol}}/L_{\text{Edd}} \geq 10$. The sources with the most extreme Eddington ratios have the highest luminosities ($L_{[\text{O III}]} \gtrsim 10^{43.5}$ erg s $^{-1}$) and lowest BH masses ($M_{\text{BH}} \approx 10^{6.5} - 10^{7.5} M_{\odot}$). Type 2 quasars, as a population, appear to have somewhat higher accretion rates than their type 1 counterparts, and the subset with the least massive BHs are radiating at highly super-Eddington rates. This may arise naturally in the evolutionary scenario linking obscured and unobscured AGNs.

5. SUMMARY

We analyze the optical spectra of the 887 low-redshift ($0.037 < z < 0.83$) type 2 quasars from the SDSS catalog of Reyes et al. (2008), with the aim of deriving two fundamental physical parameters for this population, their BH mass and Eddington ratio. Our strategy is to estimate BH masses using the $M_{\text{BH}} - \sigma_*$ relation, employing directly measured central stellar velocity dispersions whenever possible and otherwise indirectly via the velocity dispersions of the bright narrow lines [O II], [S II], and [O III].

Our main results are as follows:

1. The kinematics of the core component of the narrow emission lines trace the gravitational potential of the stars of the host galaxy, albeit with significant scatter. The low-ionization lines [S II] and [O II] are most effective, but even the high-ionization line [O III] can be used.
2. The AGN plays a secondary but still important role in governing the kinematics of narrow-line region. Narrow emission lines of both low and high ionization exhibit significantly blueshifted velocity wings. The magnitude of these nonvirial motions becomes more prominent with increasing Eddington ratio.
3. Optically selected type 2 quasars have BH masses spanning $M_{\text{BH}} \approx 10^{6.5}$ to $10^{10.4} M_{\odot}$ (median $10^{8.2} M_{\odot}$) and Eddington ratios $L_{\text{bol}}/L_{\text{Edd}} \approx 10^{-2.9}$ to $10^{1.8}$ (median $10^{-0.7}$). A minosity exceeds the Eddington limit by more than a factor of 10.
4. The accretion rates of type 2 quasars are somewhat higher than those of type 1 quasars of similar redshift.

This work was supported by the National Key R&D Program of China (2016YFA0400702), the National Science Foundation of China (11473002, 11721303), the National Youth Fund (11303008), and the Youth Foundation of Hebei Province of China (A2011205067). We thank Jenny Greene for sending the data from Greene & Ho (2005a). MK is grateful to Jian-Min Wang for his hospitality and help during her visit to IHEP and to JinLin Han for his help during her stay at NAOC. She thanks Song Huang, Ligang Hou, Xianmin Meng, Jinyi Shangguan, Jiayi Sun, and Junzhi Wang for their help.

Funding for the SDSS has been provided by the Alfred P. Sloan Foundation, the Participating Institutions, the National Science Foundation, the U.S. Department of Energy, the National Aeronautics and Space Administration, the Japanese Monbukagakusho, the Max Planck Society, and the Higher Education Funding Council for England. The SDSS Web Site is <http://www.sdss.org/>

The SDSS is managed by the Astrophysical Research Consortium for the Participating Institutions. The Participating Institutions are the American Museum of Natural History, Astrophysical Institute Potsdam, University of Basel, University of Cambridge, Case Western Reserve University, University of Chicago, Drexel University, Fermilab, the Institute for Advanced Study, the Japan Participation Group, Johns Hopkins University, the Joint Institute for Nuclear Astrophysics, the Kavli Institute for Particle Astrophysics and Cosmology, the Korean Scientist Group, the Chinese Academy of Sciences (LAMOST), Los Alamos National Laboratory, the Max-Planck-Institute for Astronomy (MPIA), the Max-Planck-Institute for Astrophysics (MPA), New Mexico State University, Ohio State University, University of Pittsburgh, University of Portsmouth, Princeton University, the United States Naval Observatory, and the University of Washington.

REFERENCES

- Abazajian, K., Adelman-McCarthy, J. K., Agüeros, M. A., et al. 2009, *ApJS*, 182, 543
- Alexandroff, R., Strauss, M. A., Greene, J. E., et al. 2013, *MNRAS*, 435, 3306
- Antonucci, R. 1993, *ARA&A*, 31, 473
- Ballantyne, D. R. 2016, *MNRAS*, 464, 626
- Barth, A. J., Ho, L. C., & Sargent, W. L. W. 2002, *AJ*, 124, 2607
- Becker, R. H., White, R. L., & Helfand, D. J. 1995, *ApJ*, 450, 559
- Beifiori, A., Maraston, C., Thomas, D. & Johansson, J. 2011, *A&A*, 531, A109
- Bender, R. 1990, *A&A*, 229, 441
- Bessiere, P., Tadhunter, C. N., Ramos Almeida, C., & Villar-Martin, M. 2012, *MNRAS*, 426, 276
- Bianchi, S., Marinucci, A., Matt, G., et al. 2017, *MNRAS*, 468, 2740
- Bruzual, G., & Charlot, S. 2003, *MNRAS*, 344, 1000
- Cappellari, M., & Emsellem, E. 2004, *PASP*, 116, 138
- Cardelli, J. A., Clayton, G. C., & Mathis, J. S., 1989, *ApJ*, 345, 245
- Dressler, A. 1984, *ApJ*, 286, 97
- Du, P., Wang, J.-M., & Zhang, Z.-X. 2017, *ApJ*, 840, L6
- Elitzur, M., & Ho, L. C. 2009, *ApJ*, 701, L91
- Elitzur, M., Ho, L. C., & Trump, J. R. 2014, *MNRAS*, 438, 3340
- Elitzur, M., & Netzer, H. 2016, *MNRAS*, 459, 585

- Ferrarese, L., & Merritt, D. 2000, *ApJ*, 539, L9
- Filippenko, A. V., & Halpern, J. P. 1984, *ApJ*, 285, 459
- Gallagher, J. S., Bushouse, H., & Hunter, D. A. 1989, *AJ*, 97, 700
- Ge, J.-Q., Hu, C., Wang, J.-M., Bai, J.-M., & Zhang, S. 2012, *ApJS*, 201, 32
- Gebhardt, K., Bender, R., Bower, G., et al. 2000, *ApJ*, 539, L13
- Gelderman, R., & Whittle, M. 1994, *ApJS*, 91, 491
- Greene, J. E., & Ho, L. C. 2005a, *ApJ*, 627, 721
- Greene, J. E., & Ho, L. C. 2005b, *ApJ*, 630, 122
- Greene, J. E., & Ho, L. C. 2006, *ApJ*, 641, 117 (GH06)
- Greene, J. E., Zakamska, N. L., Liu, X., et al. 2009, *ApJ*, 702, 441
- Halpern, J. P., & Steiner, J. E. 1983, *ApJ*, 269, L37
- Håring, N., & Rix, H.-W. 2004, *ApJ*, 604, L89
- Heckman, T. M., & Best, P. N. 2014, *ARA&A*, 52, 589
- Heckman, T., Kauffmann, G., Brinchmann, J., et al. 2004, *ApJ*, 613, 109
- Ho, L. C. 2005, *ApJ*, 629, 680
- Ho, L. C. 2008, *ARA&A*, 46, 475
- Ho, L. C. 2009, *ApJ*, 699, 638
- Ho, L. C., Filippenko, A. V., & Sargent, W. L. W. 1996, *ApJ*, 462, 183
- Ho, L. C., Filippenko, A. V., Sargent, W. L. W. 1997a, *ApJS*, 112, 315
- Ho, L. C., Filippenko, A. V., Sargent, W. L. W., & Peng, C. Y. 1997b, *ApJS*, 112, 391
- Ho, L. C., Greene, J. E., Filippenko, A. V., & Sargent, W. L. W. 2009, *ApJS*, 183, 1
- Ho, L. C., & Kim, M. 2014, *ApJ*, 789, 17
- Ho, L. C., & Kim, M. 2015, *ApJ*, 809, 123
- Ho, L. C., Kim, M., & Terashima, Y. 2012, *ApJ*, 759, L16
- Hopkins, P. F., Hernquist, L., Cox, T. J., et al. 2006, *ApJS*, 163, 1
- Kaspi S., Smith P. S., Netzer H., et al. 2000, *ApJ*, 533, 631
- Kauffmann, G., & Heckman, T. 2009, *MNRAS*, 397, 135
- Kelson, D. D., Illingworth, G. D., van Dokkum, P. G., & Franx, M. 2000, *ApJ*, 531, 159
- Kim, M., Ho, L. C., & Im, M. 2006, *ApJ*, 642, 702
- Kormendy, J., & Ho, L. C. 2013, *ARA&A*, 51, 511
- Lal, D. V., & Ho, L. C. 2010, *AJ*, 139, 1089
- Lamastra, A., Bianchi, S., Matt, G., et al. 2009, *A&A*, 504, 73
- Liu, X., Shen, Y., Strauss, M. A., & Greene, J. E. 2010, *ApJ*, 708, 427
- Liu, X., Zakamska, N. L., Greene, J. E., et al. 2009, *ApJ*, 702, 1098
- Miniutti, G., Saxton, R. D., Rodriguez-Pascual, P. M., et al. 2013, *MNRAS*, 433, 1764
- Nelson, C. H. 2000, *ApJ*, 544, L91
- Nelson, C. H., & Whittle, M. 1996, *ApJ*, 465, 96
- Netzer, H. 2015, *ARA&A*, 53, 365
- Netzer, H., Mainier, V., Rosati, P., & Trakhtenbrot, B. 2006, *A&A*, 453, 525
- Onken, C. A., Ferrarese, L., Merritt, D., et al. 2004, *ApJ*, 615, 645
- Osterbrock, D. E. 1989, *Astrophysics of Gaseous Nebulae and Active Galactic Nuclei* (Mill Valley: Univ. Science Books)
- Pennell, A., Runnoe, J. C., & Brotherton, M. 2017, *MNRAS*, 468, 1433
- Reyes, R., Zakamska, N. L., Strauss, M. A., et al. 2008, *AJ*, 136, 2373
- Sánchez-Blázquez, P., Peletier, R. F., Jiménez-Vicente, J., et al. 2006, *MNRAS*, 371, 703
- Sanders, D. B., Soifer, B. T., Elias, J. H., et al. 1988, *ApJ*, 325, 74
- Sargent, W. L. W., Schechter, P. L., Boksenberg, A., & Shortridge, K. 1977, *ApJ*, 212, 326
- Schlafly, E. F., & Finkbeiner, D. P. 2011, *ApJ*, 737, 103
- Schmidt, M., & Green, R. F. 1983, *ApJ*, 269, 352
- She, R., Ho, L. C., & Feng, H. 2017, *ApJ*, 835, 223
- Shen, Y., Greene, J. E., Ho, L. C., et al. 2015, *ApJ*, 805, 96
- Shen, Y., Richards, G. T., Strauss, M. A., et al. 2011, *ApJS*, 194, 45
- Sheth, R. K., Bernardi, M., Schechter, P. L., et al. 2003, *ApJ*, 594, 225
- Shu, X. W., Wang, T. G., Jiang, N., et al. 2017, *ApJ*, 837, 3
- Stern, J., & Laor, A. 2012, *MNRAS*, 426, 2703
- Tonry, J., & Davis, M. 1979, *AJ*, 84, 1511
- Tremaine, S., Gebhardt, K., Bender, R., et al. 2002, *ApJ*, 574, 740
- Treu, T., Woo, J.-H., Malkan, M. A., & Blandford, R. D. 2007, *ApJ*, 667, 117
- Trump, J. R., Sun, M., Zeimann, G. R., et al. 2015, *ApJ*, 811, 26
- Urry, C. M., & Padovani, P. 1995, *PASP*, 107, 803
- Valdes, F., Gupta, R., Rose, J. A., Singh, H. P., & Bell, D. J. 2004, *ApJS*, 152, 251
- Veilleux, S. 1991, *ApJS*, 75, 383
- Vestergaard, M., & Peterson, B. M. 2006, *ApJ*, 641, 689
- Whittle, M. 1985, *MNRAS*, 213, 1
- Whittle, M. 1992, *ApJ*, 387, 109
- Whittle, M., Pedlar, A., Meurs, E. J. A., et al. 1988, *ApJ*, 326, 125
- Woo, J.-H., Treu, T., Malkan, M. A., & Blandford, R. D. 2006, *ApJ*, 645, 900
- Woo, J.-H., Treu, T., Malkan, M. A., & Blandford, R. D. 2008, *ApJ*, 681, 925

Zakamska, N. L., Gomez, L., Strauss, M. A., & Krolik, J.
H. 2008, AJ, 136, 1607
Zakamska, N. L., Lampayan, K., Petric, A., et al. 2016,
MNRAS, 455, 4191

Zakamska, N. L., Strauss, M. A., Krolik, J. H., et al. 2003,
AJ, 126, 2125
Zhao, D., Ho, L. C., Zhao, Y.-Li., Kim, M., & Shangguan,
J. 2018, in preparation

Table 1. Sample Properties

Object Name	z	A_V	S/N	EW	$H\alpha/H\beta$	$L_{[\text{O III}]}$	σ_*	$\sigma_{[\text{S II}]}$	$\sigma_{[\text{O II}]}$	$\sigma_{[\text{O III}]}$	$\sigma_{[\text{S II}]}$	$\sigma_{[\text{O II}]}$	$\sigma_{[\text{O III}]}$	M_{BH}	$L_{\text{bol}}/L_{\text{Edd}}$
SDSS		(mag)		(Å)		(erg s^{-1})	(km s^{-1})	(km s^{-1})	(km s^{-1})	(km s^{-1})	(km s^{-1})	(km s^{-1})	(km s^{-1})	(M_{\odot})	
(1)	(2)	(3)	(4)	(5)	(6)	(7)	(8)	(9)	(10)	(11)	(12)	(13)	(14)	(15)	(16)
J000259.10+004018.1	0.6007	0.0762	4.1	< 3	4.04	43.13±0.05	136.0±23.2	...	343.1±5.3	464.9±28.6	7.76±0.80	0.05±0.81
J000351.83-010142.0	0.2689	0.0968	7.1	5.4	4.04	42.19±0.05	241.7±65.5	225.4±63.7	...	284.9±27.7	276.9±32.4
J000453.43-005038.4	0.6430	0.1100	3.1	< 3	4.04	43.31±0.05	137.3±9.8	174.0±2.0	...	382.6±15.8	500.5±42.0	7.66±0.75	0.33±0.76
J000728.83+010604.0 ^a	0.4663	0.0988	7.8	6.0	4.04	42.37±0.05	203.4±50.6	599.3±104.7	402.0±93.1
J001000.75-011008.5	0.5823	0.0936	6.1	< 3	4.04	42.71±0.06	392.6±57.1	204.4±59.0	...	504.4±41.9	260.1±13.8	9.69±0.79	-2.30±0.80
J001111.95+005626.3	0.4094	0.0812	6.9	< 3	4.04	42.69±0.05	133.6±17.5	138.7±31.6	...	414.3±43.0	289.6±19.4	7.61±0.78	-0.25±0.79
J001126.95+155329.6	0.0999	0.2062	12.3	5.5	3.76±0.05	42.14±0.02	154.9±19.4	141.2±5.9	159.1±8.2	134.9±5.5	247.6±31.3	225.5±18.2	224.0±6.7	8.01±0.37	-1.19±0.39
J001206.31-094725.6	0.1668	0.1057	13.8	5.2	5.17±0.22	42.92±0.06	146.7±21.2	114.0±7.4	167.5±43.9	154.0±7.4	242.0±11.5	423.1±34.3	285.0±18.4	7.90±0.40	-0.30±0.42
J002016.88-093244.7	0.3600	0.1289	20.9	< 3	5.17±0.31	43.06±0.08	182.9±8.5	176.0±4.2	...	376.3±31.7	469.9±4.2	8.22±0.74	-0.48±0.75

NOTE—
^aKinematically complex emission-line core.
Column (1): SDSS name. Column (2): Redshift. Column (3): Extinction in the V band. Column (4): Average S/N per pixel over the region 4400 – 4600 Å. Column (5): EW of the G band. Column (6): Observed Balmer decrement used to estimate internal extinction. Objects for which the Balmer decrement could not be reliably determined are assigned a value of $H\alpha/H\beta = 4.04$, the median of the detected objects. Column (7): Extinction-corrected luminosity of [O III] $\lambda 5007$. The uncertainties include measurement error and uncertainties of the Balmer decrement. Column (8): Stellar velocity dispersion. Columns (9)–(11): Gaseous velocity dispersion of the core component of [S II] $\lambda\lambda 6716, 6731$, [O II] $\lambda\lambda 3726, 3729$, and [O III] $\lambda 5007$. Columns (12)–(14): Second moment of the line profile of [S II] $\lambda\lambda 6716, 6731$, [O II] $\lambda\lambda 3726, 3729$, and [O III] $\lambda 5007$. Column (15): BH mass estimated from the $M_{\text{BH}} - \sigma_*$ relation of Kormendy & Ho (2013; Equation 2), using, in the order of preference, σ_* , $\sigma_{[\text{S II}]}$, $\sigma_{[\text{O II}]}$, and $\sigma_{[\text{O III}]}$, with σ_g^c statistically corrected as described in Section 4.3. Column (16): Eddington ratio calculated with extinction-corrected [O III] luminosity (Col. 7) and BH mass (Col. 15). Uncertainties introduced by the bolometric correction are included in the error budget. *This table is available in its entirety in a machine-readable form in the on-line journal. A portion is shown here for guidance regarding its form and content.*

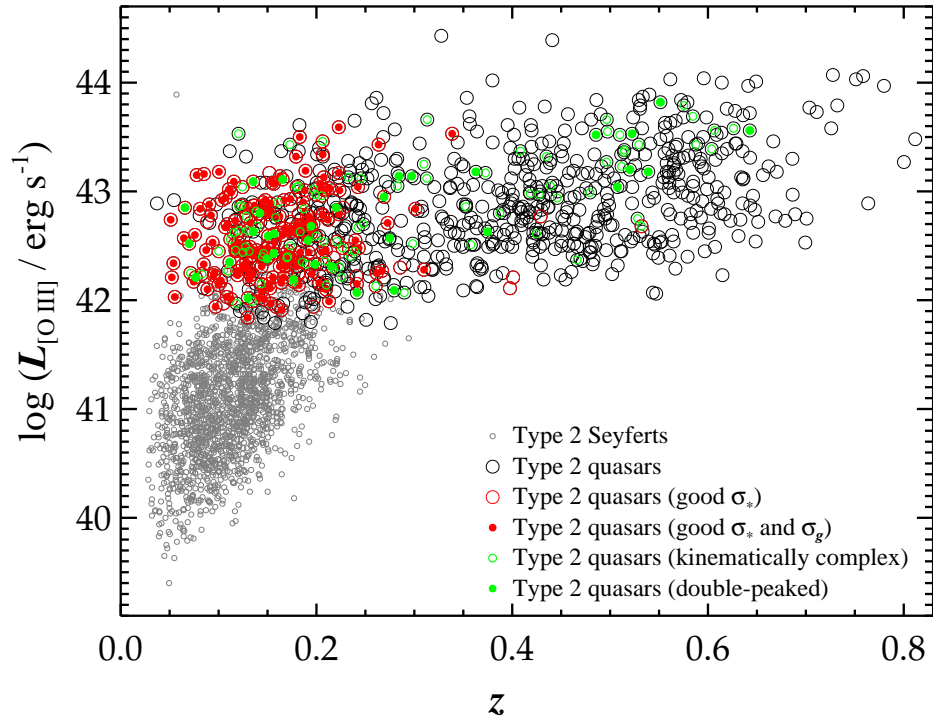


Figure 1. Distribution of [O III] luminosities and redshifts of our parent sample of 887 type 2 quasars (open black symbols). Plotted in red are the 219 objects that have σ_* measurements with fractional errors $\leq 20\%$, with the final sample of 142 objects having robust values of both σ_* and σ_g further highlighted as filled red symbols. Green symbols denote objects with kinematically complex emission-line cores, and green filled symbols mark the subset with double-peaked profiles. The small grey points are the lower luminosity type 2 AGNs (Seyferts) from Greene & Ho (2005a).

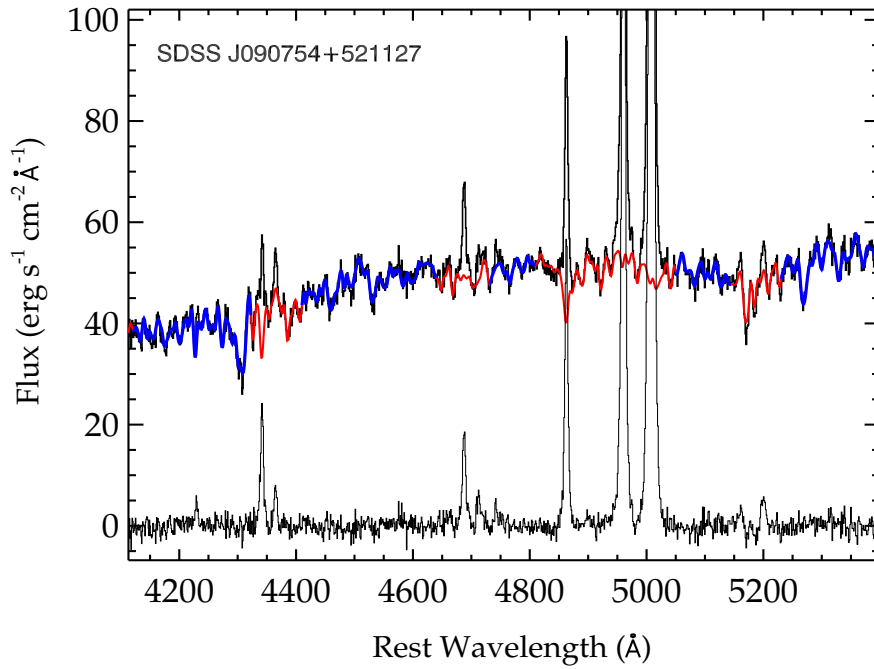


Figure 2. Illustration of the method for σ_* measurement. The SDSS spectrum, corrected for extinction and redshift, is plotted as thick black histograms. The best-fit model, a scaled, broadened composite stellar template comprising several individual stars (F, K, and M late-type red giants), is plotted in blue. Regions of the spectrum containing strong emissions are excluded from the fit (red). The residuals (data minus best-fit model) are plotted on the bottom.

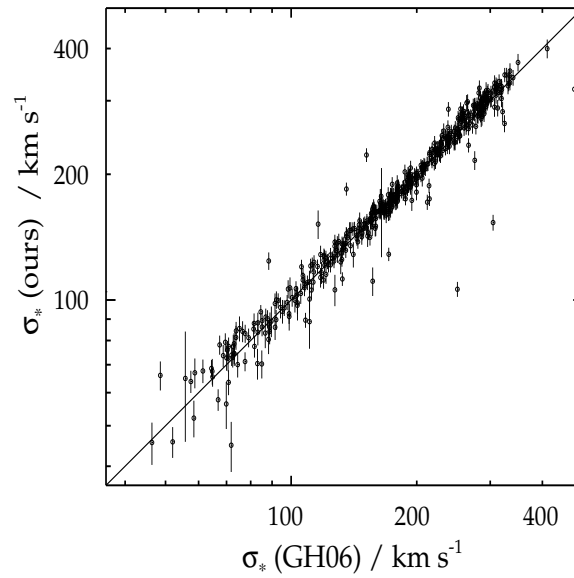


Figure 3. Comparison between our measurements of σ_* and those of GH06 for their reference sample of 504 active galaxies. The agreement is excellent. The mean difference between the two sets of measurements is $\langle \Delta \sigma_* \rangle = 0.002 \pm 0.05$, where $\Delta \sigma_* \equiv \log \sigma_*(\text{ours}) - \log \sigma_*(\text{GH06})$.

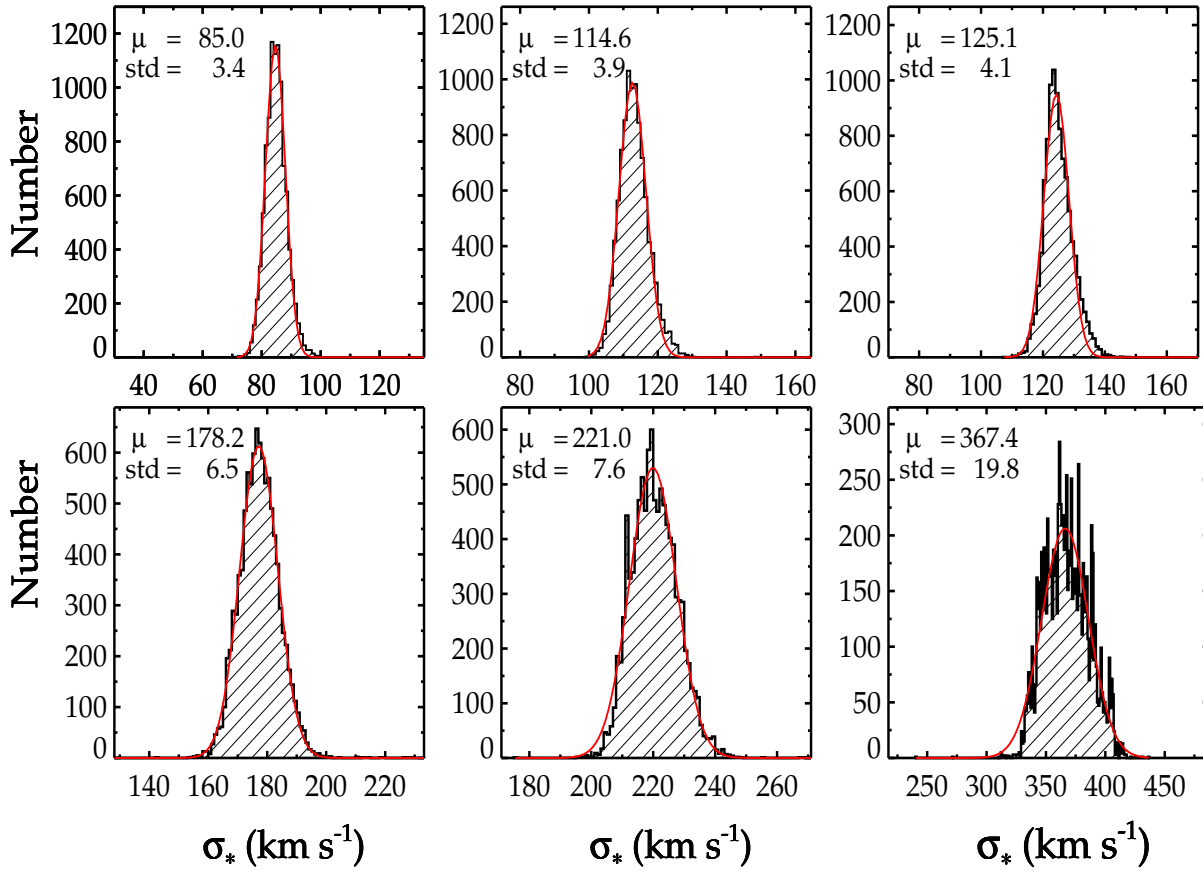


Figure 4. The effect of template mismatch on measured velocity dispersions. For each of six high-S/N ($\gtrsim 90$) SDSS galaxy spectra with $\sigma_* = 85, 114, 125, 178, 220,$ and 360 km s^{-1} , we perform 10^4 fits with different stellar templates constructed from random combinations of stars with spectral type A, F, G, K, and M. The mean (μ) of the resulting distribution of σ_* and its standard deviation from a Gaussian fit (red line) to the distribution are given in the top left corner of each panel.

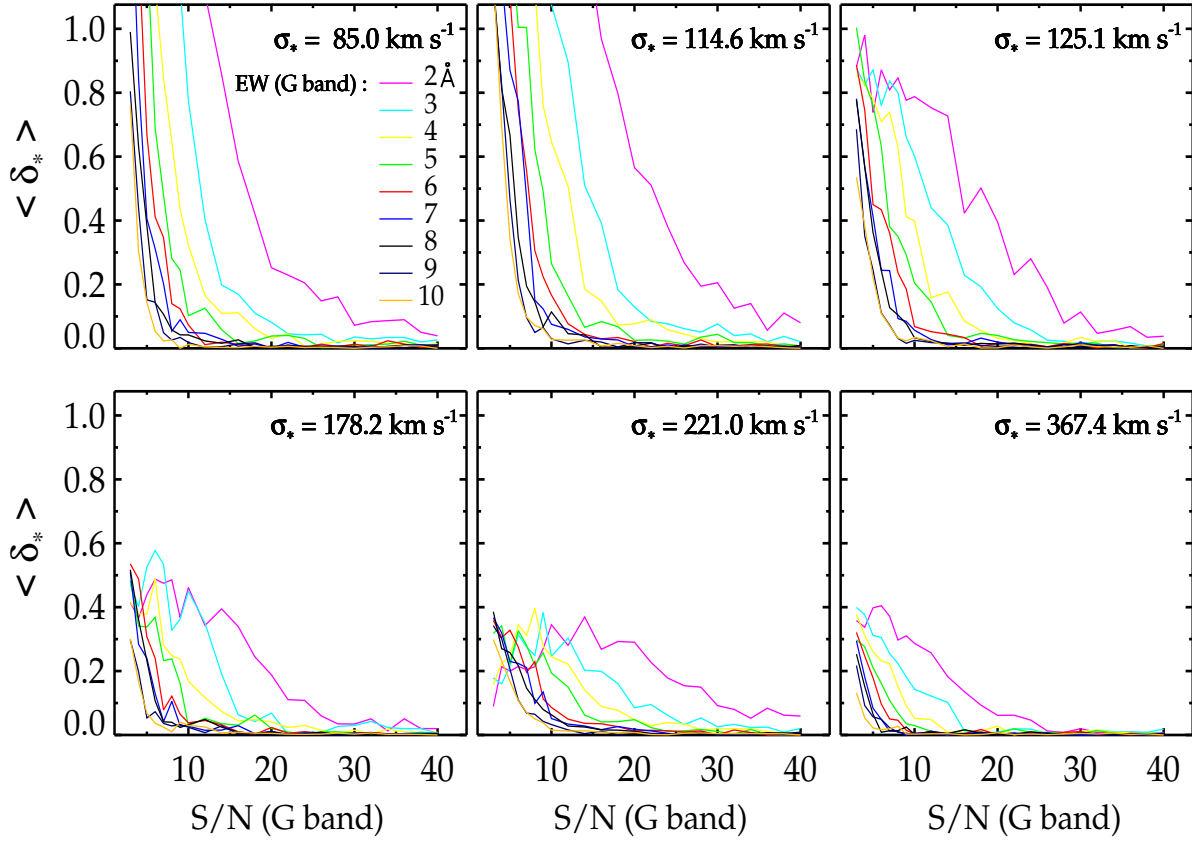


Figure 5. Systematic errors on the measured stellar velocity dispersions introduced by S/N and strength (EW) of the G band stellar feature. The panels show simulations performed on six high-S/N ($\gtrsim 90$) SDSS galaxy spectra with $\sigma_* = 85, 114, 125, 178, 220,$ and 360 km s^{-1} . The mean fractional error on σ_* is given as $\langle \delta \sigma_* \rangle = \langle [\sigma_*(\text{input}) - \sigma_*(\text{output})] / \sigma_*(\text{input}) \rangle$, for different combinations of S/N and EW(G band).

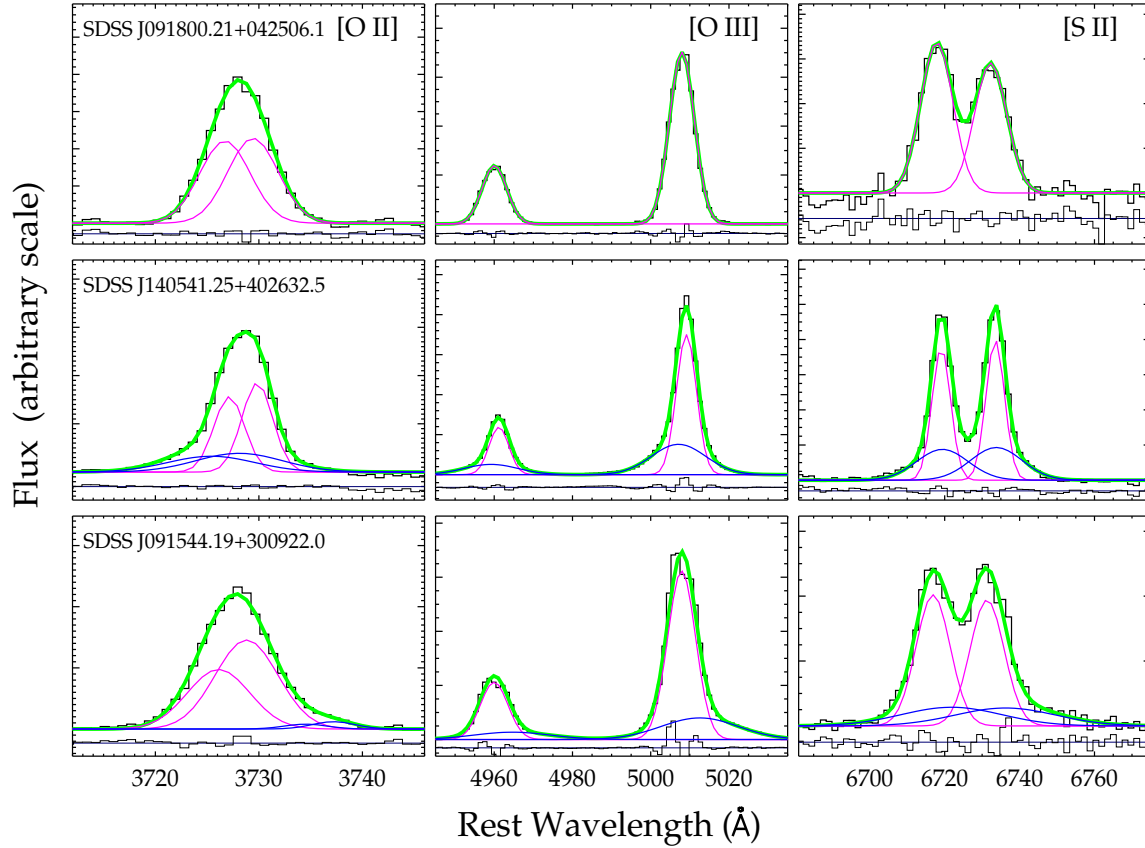


Figure 6. Sample fits for the emission lines (left) [O II] $\lambda\lambda 3726, 3729$, (middle) [O III] $\lambda\lambda 4959, 5007$, and (right) [S II] $\lambda\lambda 6716, 6731$. The top object requires only a single Gaussian component for each line, whereas the lines for the other two objects each require two components, one whose wing is blueshifted (middle row) and the other that is redshifted (bottom row). The data are plotted in black, the best-fit model in green, and individual components in magenta (core) and blue (wing). The residuals (data minus model) are plotted on the bottom of each panel as thin black histograms.

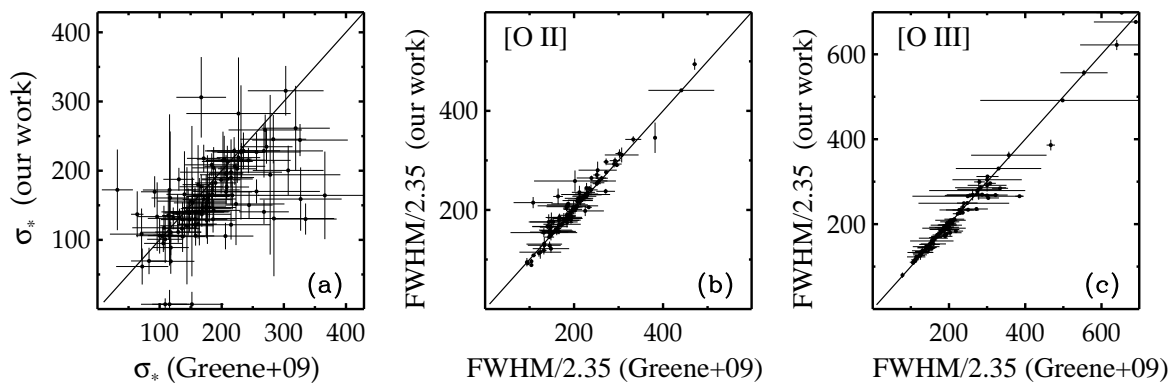


Figure 7. Comparison of our measurements with those of Greene et al. (2009) for (a) σ_* , (b) FWHM of [O II], and (c) FWHM of [O III]. The solid line denotes the 1:1 relation.

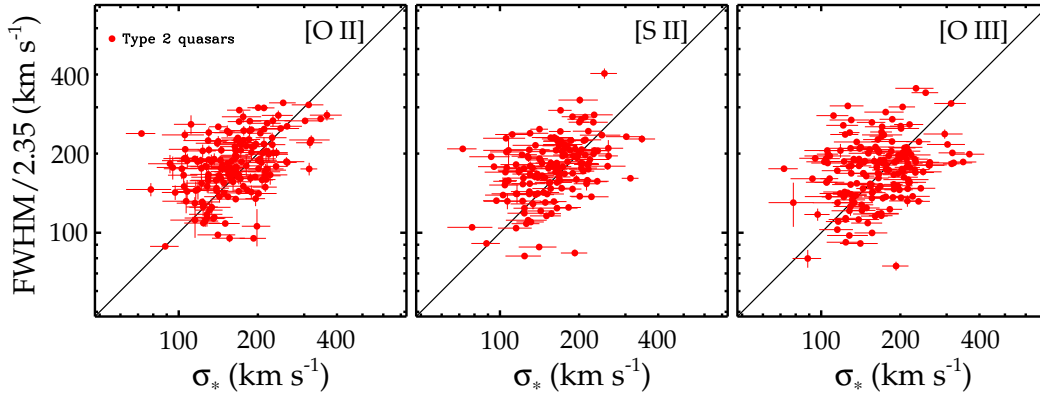


Figure 8. Comparison of stellar velocity dispersions σ_* with gaseous velocity dispersions estimated from FWHM/2.35 of the [O II], [S II], and [O III] narrow emission lines. The data consist of the subset of type 2 quasars in this study having velocity dispersions measurements with fractional uncertainties $\leq 20\%$. The solid line denotes the 1:1 relation.

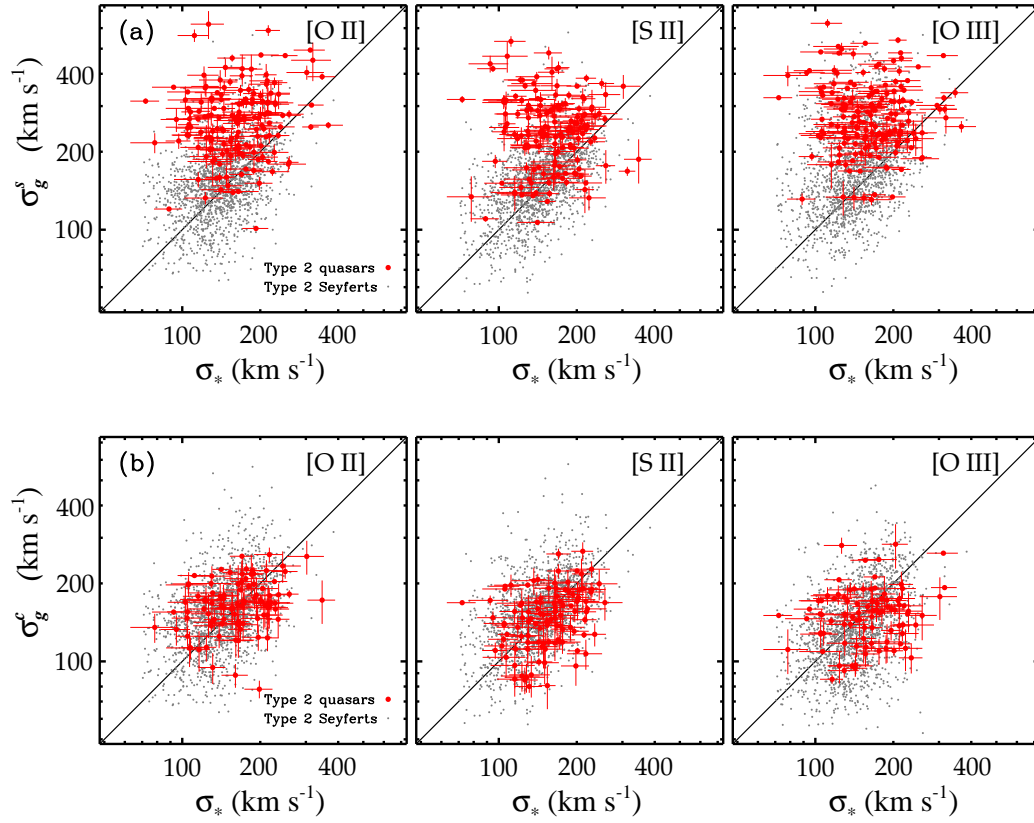


Figure 9. Comparison of stellar velocity dispersions σ_* with gaseous velocity dispersions for the (left) [O II], (middle) [S II], and (right) [O III] emission lines measured from (a) the second moment (σ_g^s) and (b) the core (σ_g^c) of the line profile. The small grey points are from the lower luminosity type 2 AGNs (Seyferts) from Greene & Ho (2005a). The red points with error bars are the subset of type 2 quasars in this study with fractional uncertainties $\leq 20\%$. The solid line denotes the 1:1 relation.

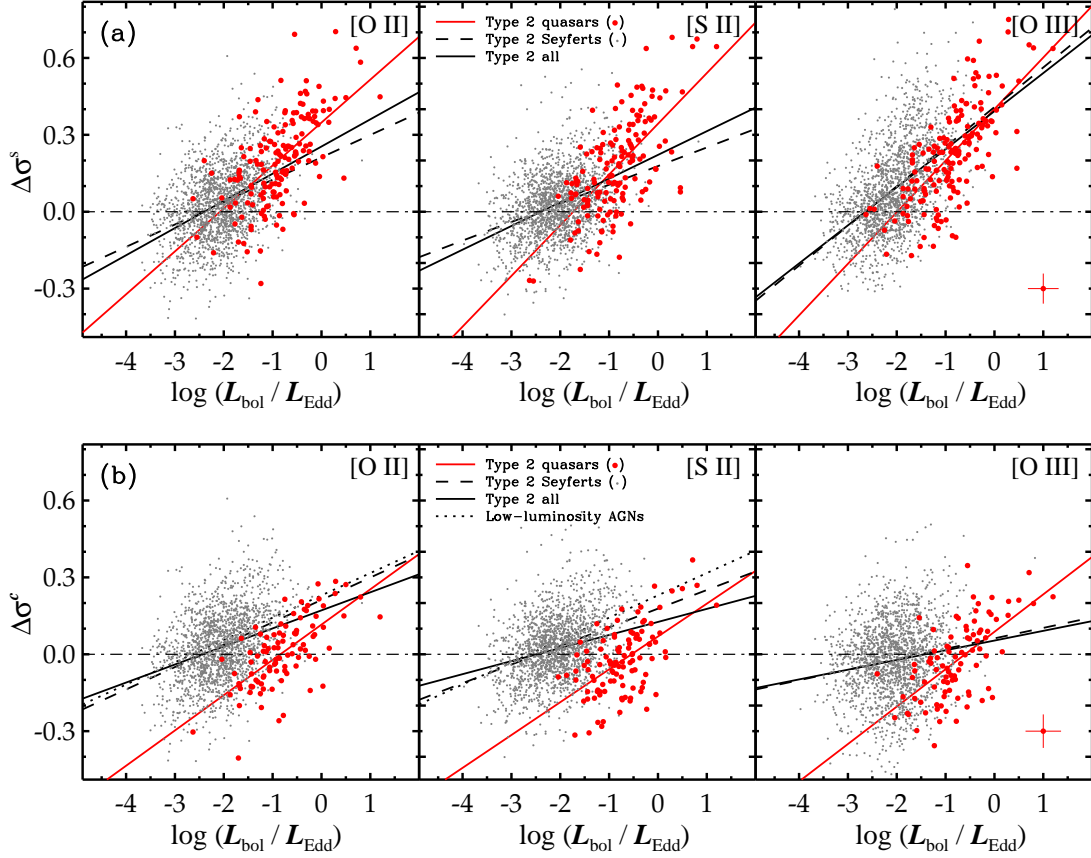


Figure 10. The relation between $L_{\text{bol}}/L_{\text{Edd}}$ and (a) $\Delta\sigma^s \equiv \log \sigma_g^s - \log \sigma_*$ and (b) $\Delta\sigma^c \equiv \log \sigma_g^c - \log \sigma_*$ for (left) [O II], (middle) [S II], and (right) [O III]. The small grey points are the lower luminosity type 2 Seyferts from Greene & Ho (2005a). The red points are the subset of type 2 quasars in this study with fractional uncertainties $\leq 20\%$; individual error bars are omitted for clarity, but a representative error bar is shown on the bottom-right corner of the [O III] plot. Best-fit relations, calculated using an ordinary least-squares regression with $L_{\text{bol}}/L_{\text{Edd}}$ as the independent variable, are given for the type 2 quasars (solid red line), type 2 Seyferts (dashed black line), and type 2 Seyferts and quasars combined (solid black line). For comparison, the relation derived by Ho (2009; his Equation 3) for [N II] $\lambda 6583$ is overplotted as a dotted black line in the [O II] and [S II] plots of panel (b).

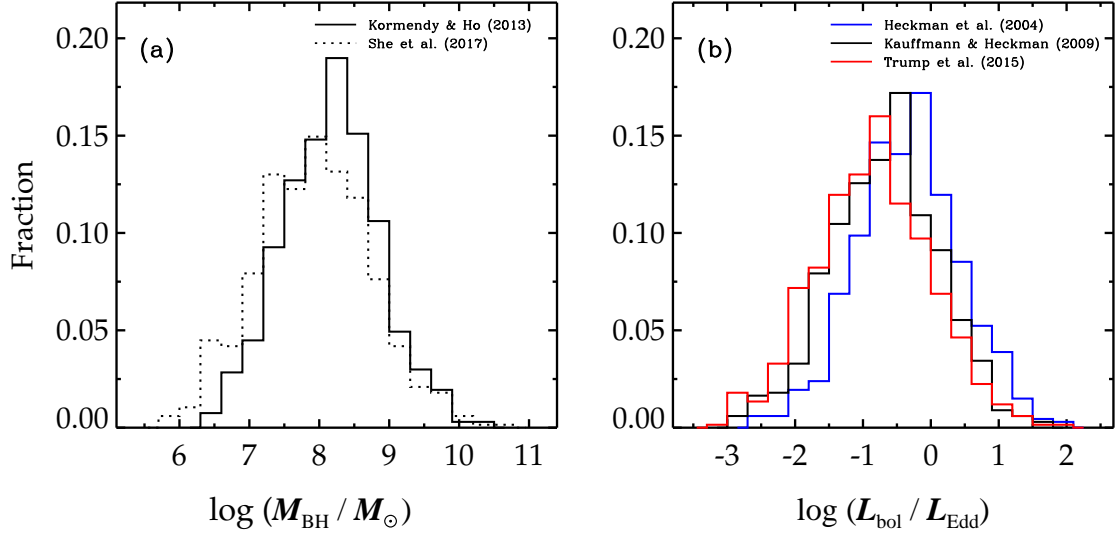


Figure 11. (a) Distribution of BH masses for our sample of type 2 quasars. The solid histograms assume the $M_{\text{BH}} - \sigma_*$ relation for classical bulges and elliptical galaxies (Equation 2; Kormendy & Ho 2013); the dotted histograms use the $M_{\text{BH}} - \sigma_*$ relation for all bulge types (see footnote 7; She et al. 2017). (b) Distribution of Eddington ratios assuming the $M_{\text{BH}} - \sigma_*$ relation for classical bulges and elliptical galaxies and the [O III] bolometric correction of Heckman et al. (2004; blue), Kauffmann & Heckman (2009; black), and Trump et al. (2015; red), which is based on a power-law fit to the data from Lamastra et al. (2009).

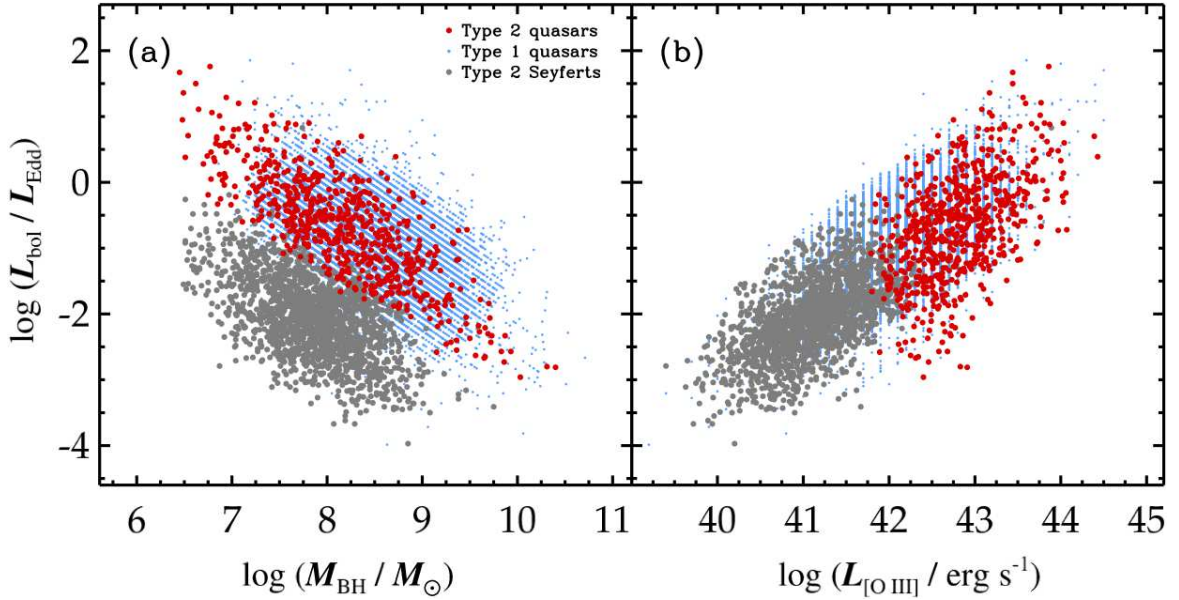


Figure 12. Distribution of Eddington ratio versus (a) BH mass and (b) [O III] luminosity for our sample of type 2 quasars (red points), lower luminosity, lower redshift type 2 Seyferts from Greene & Ho (2005a; grey points), and type 1 quasars with $z < 0.83$ from Shen et al. (2011; blue points).